

Article

Quantitative Phase Fraction Detection in Organic Photovoltaic Materials through EELS Imaging

Ondrej Dyck^{1,*}, Sheng Hu¹, Sanjib Das², Jong Keum³, Kai Xiao³, Bamin Khomami¹ and Gerd Duscher⁴

Received: 24 August 2015; Accepted: 17 November 2015; Published: 24 November 2015

Academic Editors: Christian Nielsen and Laure Biniek

¹ Department of Chemical and Biomolecular Engineering, University of Tennessee, Knoxville, TN 37996, USA; shu@vols.utk.edu (S.H.); bkhomami@utk.edu (B.K.)

² Department of Electrical Engineering and Computer Science, University of Tennessee, Knoxville, TN 37996, USA; sdas8@vols.utk.edu

³ Center for Nanophase Materials Sciences/Spallation Neutron Source, Oak Ridge National Laboratory, Oak Ridge, TN 37831, USA; keumjk@ornl.gov (J.K.); xiaok@ornl.gov (K.X.)

⁴ Department of Materials Science and Engineering, University of Tennessee, Knoxville, TN 37996, USA; gduscher@utk.edu

* Correspondence: Odyck@utk.edu

Abstract: Organic photovoltaic materials have recently seen intense interest from the research community. Improvements in device performance are occurring at an impressive rate; however, visualization of the active layer phase separation still remains a challenge. This paper outlines the application of two electron energy-loss spectroscopic (EELS) imaging techniques that can complement and enhance current phase detection techniques. Specifically, the bulk plasmon peak position, often used to produce contrast between phases in energy filtered transmission electron microscopy (EFTEM), is quantitatively mapped across a sample cross section. A complementary spectrum image capturing the carbon and sulfur core loss edges is compared with the plasmon peak map and found to agree quite well, indicating that carbon and sulfur density differences between the two phases also allows phase discrimination. Additionally, an analytical technique for determining absolute atomic areal density is used to produce an absolute carbon and sulfur areal density map. We show how these maps may be re-interpreted as a phase ratio map, giving quantitative information about the purity of the phases within the junction.

Keywords: phase detection; organic photovoltaics; plasmon energy mapping; electron energy loss spectroscopy; EELS Core-loss mapping; EFTEM

1. Introduction

Recent years have seen an increasing interest in organic photovoltaics (OPV) [1–3]. As a result, there is a high scientific demand for microstructural characterization of the various fabricated devices [2]. Here, we introduce several techniques for examining OPV materials in a (scanning) transmission electron microscope ((S)TEM) instrument capable of electron energy-loss spectroscopy (EELS). The prototypical materials under investigation are P3HT, PTB7 and PCBM. These materials are good candidates for demonstrating the fidelity of carbon density phase detection due to their different carbon densities (71 carbon atoms/nm³ for PCBM, 38 carbon atoms/nm³ for PTB7, and 42 carbon atoms/nm³ for P3HT, discussed later). Although this study is material specific, the techniques discussed can certainly lend themselves to other material systems given that either the densities of elements are different between the two materials or a unique identifying element exists in one of the materials.

Organic materials exhibit poor contrast in TEM due to their low Z number and fairly uniform densities [2]. Energy filtered TEM (EFTEM) is an increasingly common method for enhancing contrast in organic materials. This is accomplished by introducing a post-specimen energy window that only allows electrons having a specific range of energies form the image [4–11]. The motivation behind the use of this technique is that the different materials within the bulk heterojunction (BHJ) have plasmon losses at different energies. For example, in the P3HT/PCBM system, positioning the energy window at 19 eV will cause the P3HT to brighten and the PCBM to darken. Positioning an energy window at 30 eV will cause the PCBM to brighten and the P3HT to darken [6]. Hence, an artificially colored composite of these two images provides a clear contrast between the components.

One of the drawbacks of this method is that it is a projection. A second drawback is that it is a qualitative measurement. Together, these can distort one's perception of the actual structures in the material. Intensities are linked to a predominance of one material or another, but this says nothing about purity. For example, if one were to examine a sample and find areas of high PCBM concentration the natural interpretation would be to assume these are PCBM aggregations in a network of donor polymers. However, this same picture can be interpreted as an interconnected donor polymer web in a PCBM matrix. Without knowing purity (or the volume fraction) of each constituent polymer, these two cases become indistinguishable. EFTEM tomography alleviates the problem of projection and is thereby able to distinguish between these two cases but still lacks quantitative information about purity. This technique is also technically challenging and has seen limited use in the investigation of OPV material systems.

In this study, we explore an alternative material detection mechanism that allows for a quantitative measurement of the fraction of each material. In the first part of the paper we show how this can be accomplished, given a few assumptions, with a spectrum image that captures the carbon K edge. Using this technique we find evidence for a mixed phase in a P3HT/PCBM system. We then outline a further refinement of the technique that relies on both the carbon K edge and the sulfur L_{23} edge. With an additional measurement, fewer assumptions are required and a comparison of several calculations allows limiting the measurement errors to $\pm 20\%$. Here, we illustrate the detection of a PTB7 web in a PCBM matrix rather than what initially appears to be PCBM aggregates in a PTB7 matrix.

2. Experimental Section

2.1. Materials and Device Fabrication

Two material systems were investigated in this study: P3HT/PCBM and PTB7/PCBM.

P3HT/PCBM system: Regio-regular poly(3-hexylthiophene) (P3HT) and [6,6]-phenyl C_{61} -butyric acid methyl ester (PCBM) (99.5%) were purchased from Rieke Metals Inc. (Lincoln, NE, USA), and Nano-C Inc. (Westwood, MA, USA), respectively.

The substrates used were silicon wafers first cleaned in hot piranha (3:1 $H_2SO_4:H_2O_2$) at 60 °C for 30 min, then washed in deionized (DI) water and dried under nitrogen gas. P3HT:PCBM (in a weight ratio of 1:0.8) was then dissolved in *o*-dichlorobenzene (ODCB) to achieve a solution with P3HT and PCBM concentrations of 10 mg/mL and 8 mg/mL, respectively. Spin coating this solution on the substrate produced ~ 70 nm thick films. Subsequent solvent vapor annealing in Toluene was performed for 1 h at 90% of the solvent vapor pressure to enhance phase separation. The device exhibited a $J_{sc} = 5.193$ mA/cm², $V_{oc} = 0.547$ V, $FF = 47.8\%$, and a $PCE = 1.36\%$. Additional details may be found in a separate publication [12].

PTB7/PCBM system: Poly(4,8-bis[(2-ethylhexyl)oxy]benzo[1,2-b:4,5-b']dithiophene-2,6-diyl 3-fluoro-2-[(2-ethylhexyl)carbonyl]thieno[3,4-b]thiophenediyl) (PTB7) and PC₇₁BM were purchased from 1-Material (Dorval, Quebec, Canada) and Nano-C, respectively, and used as received. The PTB7:PC₇₁BM blend solution was prepared by dissolving PTB7 and PC₇₁BM (with 1:1.5 ratio and 25 mg/mL total concentration) in dichlorobenzene and heating at 70 °C for several hours.

Silicon substrates were first cleaned by detergent and subsequently sonicated in DI water, acetone, and isopropyl alcohol (IPA) followed by baking at 80 °C for one hour. The poly-[(9,9-bis(3'-(*N,N*-dimethylamino)propyl)-2,7-fluorene)-alt-2,7-(9,9-dioctylfluorene)] (PFN) solution was prepared by dissolving PFN in methanol (2 mg/mL) with the presence of a small amount of acetic acid, and spun cast onto the substrates at 3000 rpm. The active layer was spun cast at 1000 rpm for 90 s followed by drying for 30 min in an inert environment. For device performance measurements, indium tin oxide (ITO) coated glass substrates were used and the device was completed by thermally depositing 8 nm of MoO₃ and 100 nm of Ag. The device exhibited a $J_{sc} = 15.3 \text{ mA/cm}^2$, $V_{oc} = 0.72 \text{ V}$, $FF = 46.9\%$, and a $PCE = 5.2\%$. Additional details may be found in a separate publication [13].

2.2. Transmission Electron Microscopy

Transmission electron microscopy (TEM) studies were performed using a Zeiss Libra 200 MC TEM (Carl Zeiss AG: Oberkochen, Germany). This TEM is equipped with an energy filter and monochromator and was operated at an accelerating voltage of 200 kV.

Cross-section samples were prepared using a Zeiss Auriga Crossbeam focused ion beam (FIB) microscope (Carl Zeiss AG: Oberkochen, Germany). A one micron Pt sacrificial layer was deposited over the sample surface before milling to protect the polymers. Rough milling was performed at 30 kV 2 nA to extract a lamella about 2 μm thick from the bulk sample. This lamella was mounted onto a Cu finger grid and a final polish at 10 kV 10 pA was used to thin the lamella below 100 nm.

Energy filtered TEM (EFTEM) images have previously shown successful determination of phase separation in similar bulk heterojunctions [2,4–7]. Following the techniques described in earlier studies, EFTEM images were taken with a slit width of 8 eV centered at 19 and 30 eV. Artificial coloring was added and the EFTEM images were overlaid to enhance visualization of the phases.

The spectrum image represented in Figure 3 was acquired with a beam current of 48 pA, an exposure time of 0.2 s per pixel, a pixel dimension of 5 nm² with subpixel scanning and energy resolution of 0.56 eV. The convergence angle was 9 mrad and collection angle was 54 mrad. The spectrum image represented in Figure 7 was acquired with a beam current of 18 pA, an exposure time of 0.3 s per pixel, a pixel dimension of 5 nm² with subpixel scanning and an energy resolution of 0.9 eV. The convergence angle was 9 mrad and collection angle was 30 mrad.

2.3. Data Analysis

Low loss EELS data was fit with a Gaussian distribution by a least squares fitting routine. The zero loss peak (ZLP) was approximated by the sum of a Gaussian and Lorentzian distribution.

The core loss data was fit with a background subtraction routine of the form $E^{-r} + aE^2 + bE + c$ which represents a power law decay modified by a polynomial to allow for slight deviations in the data from a true power law [14]. Concurrently, a hydrogenic partial scattering cross section model was used to fit the core loss edges. Additionally, a representative low loss spectrum of the same area was convolved with the hydrogenic scattering cross section to more accurately fit the edge and account for features due to plural scattering.

In order to obtain quantitative elemental measurements, the scattering probability must be calculated. Once the background was subtracted from a core loss edge, the area under the edge was used as an estimate of the total scattering probability for that element. Scattering probabilities for single atoms are well known [15] and dividing the measured scattering probability by the known scattering probability produces the number of atoms (of that element) under the beam.

$$N_{atoms} = \frac{N_s / N_{tot}}{P_s} \quad (1)$$

Here, N_{atoms} is the number of atoms under the beam, N_{tot} is the number of incident electrons, N_s is the number of scattered electrons (area under the EELS edge), and P_s is the probability of scattering from a single atom. For further discussion, see Egerton [14].

3. P3HT/PCBM System: Results and Discussion

3.1. EFTEM Imaging

In order to give a baseline comparison for the EELS imaging results, EFTEM imaging was performed to distinguish between P3HT and PCBM. Figure 1 represents a typical EFTEM image from the sample. We can clearly distinguish between the P3HT and PCBM rich areas. The PCBM rich area in this sample aggregates near the Si substrate.

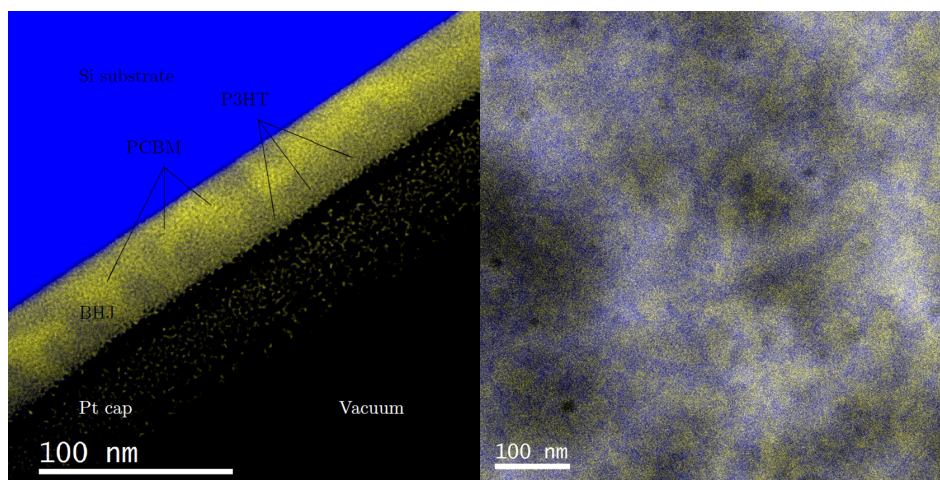


Figure 1. An artificially colored composite of two EFTEM images highlight intensity variations arising from a change in the bulk plasmon energy between P3HT and PCBM. The EFTEM image with the slit centered on 19 eV is colored blue while the EFTEM image with the slit centered at 30 eV is colored yellow. (Left) is a cross-section of the BHJ film shown in plan view on the (right). The Si substrate appears blue due to the large bulk plasmon peak of Si near the 19 eV energy window.

One of the caveats for using the bulk plasmon for this type of imaging is that many materials have bulk plasmons in similar ranges. For example silicon has a sharp bulk plasmon peak at ~ 19 eV which falls precisely in the energy range usually used to detect P3HT. In Figure 1 we can see that this causes the silicon to exhibit a strong “P3HT” signal. This is not a problem in this case because the silicon plasmon location is known, however the introduction of contaminant materials [16] or unexpected variations in the bulk plasmon could easily distort EFTEM images. For this reason, recorded spectra should accompany EFTEM imaging. Ideally, an EELS image should be used to perform precise analysis of spectral variations with sample position post-acquisition.

3.2. EELS Imaging

EELS images were also taken of the cross-section samples. With this technique, the electron beam is slowly rastered across the sample and an EELS spectrum is recorded at each position. Figure 2 shows one such spectrum from a spectrum image fitted with two Gaussian distributions to capture the position of the bulk plasmon peak.

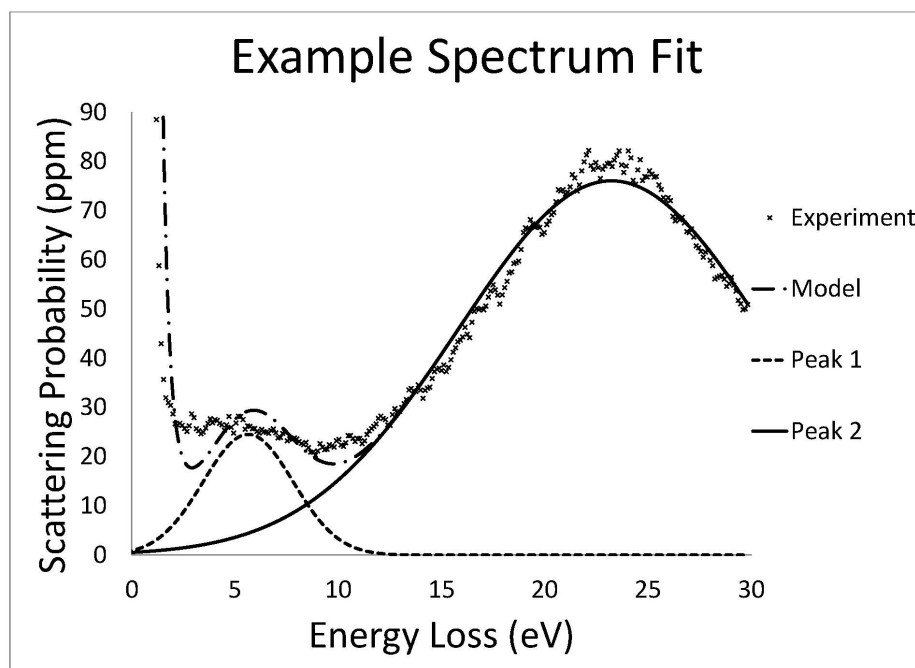


Figure 2. Example fit of a single spectrum from the EELS spectrum image. Peak 2 captures the bulk plasmon peak position which is mapped across the sample in Figure 3a.

The movement of the bulk plasmon peak labeled “Peak 2” is responsible for the intensity variations highlighted in the EFTEM images (Figure 1). This peak position shifts by about 1 eV depending upon which material the beam is incident, Figure 3a. The color in Figure 3a shows the energy position of peak 2 while the x and y dimensions represent physical position on the sample. It should be noted that peak 1 was merely used so that the fitting algorithm did not attempt to use peak 2 to represent data below ~ 15 eV. Additional peaks do improve the fit in the low energy range but are unnecessary for accurate fitting of the bulk plasmon. Peak 2 does indeed capture the bulk plasmon peak quite well so the position measurements for this peak are well represented. It is not surprising that this produces similar results to the EFTEM image since they both rely on the same spectral feature changes.

The EELS plasmon map is not a completely independent measurement technique from EFTEM imaging as it also relies upon the movement of the plasmon peak to differentiate the component materials. Specifically, this measurement seems to indicate a PCBM-rich layer at the surface of the sample as seen in Figure 3a. We know that there is also a layer of platinum somewhere in this region so it is unclear whether this signal is truly from PCBM. A second method is needed to confirm this observation.

In order to obtain a completely independent measurement, we noted that the carbon density in P3HT is about half that of the carbon density in PCBM. We calculated carbon density by multiplying the carbon weight percent, obtained from the linear formulas, by the density of each material and converting it to appropriate units. For P3HT, we used the linear formula $C_{10}H_{14}S$, and density of 1.15 g/mL, to predict a carbon concentration of 42 atoms/nm³. For PCBM we used the linear formula, $C_{72}H_{14}O_2$, and a density of 1.6 g/mL to calculate a carbon concentration of 76.2 atoms/nm³.

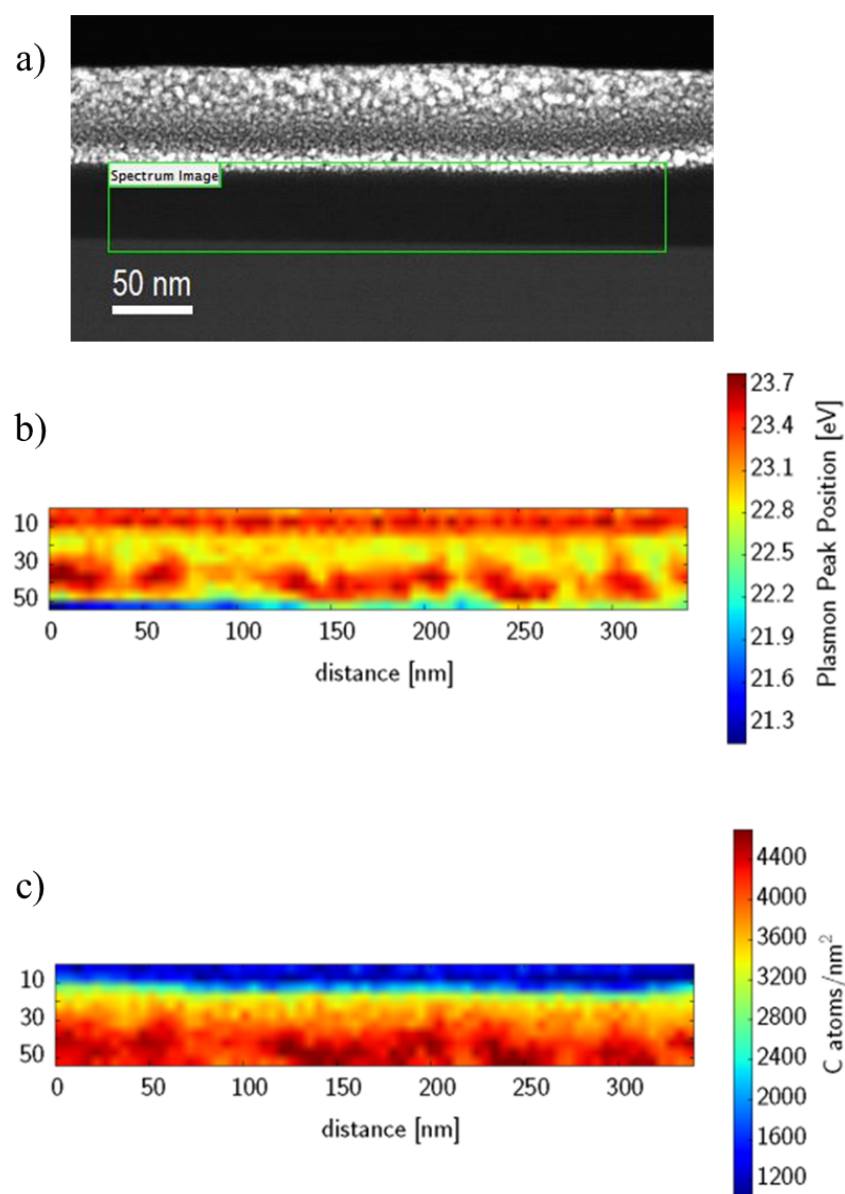


Figure 3. (a) High angle annular dark field image of the acquisition area. During EELS acquisition the sample drifted down by a few nanometers as is evident in (b,c); (b) Quantitative view of the plasmon peak shift between the PCBM rich and P3HT rich phases. The Si substrate is at the bottom of the image. The PCBM rich area is found where the plasmon peak shifts to higher values near the substrate. The top layer that generates a signal similar to that of PCBM has a very low carbon concentration and is attributed to the platinum protective layer deposited during sample preparation. (c) Carbon areal density measured across the same area as in (b) (a small vertical drift is present). The higher carbon density areas closely match with the plasmon peak position shift. The agreement between (b) and (c) gives credence to the techniques. The plasmon signal at the top in (a) highlights the possible misinterpretation of the plasmon variations which make this area appear as a high PCBM concentration area, yet (b) shows a sharp reduction in carbon concentration.

It is important to note that these density values are rather rough estimates taken from measured literature values. Table 1 shows a few of these values and we see there is a significant spread, particularly in the density of PCBM. While many reports simply assert a density of 1.5 g/cm^3 with little to no experimental support, all but a single study show PCBM to be 1.6 g/cm^3 when care

is taken to actually measure the density. For this reason, we used 1.6 g/cm^3 in our calculations. It seems likely that processing parameters play a significant role in the final density and that one may even find a range of densities within the same sample due to (for example) degree of crystallinity. Future refinements of this technique may heighten the precision such that these small density fluctuations become apparent (and their detection would be quite revealing). Indeed, precision density measurements on a nanometer scale should be possible on a specimen of known thickness (on a single, uniform material). In this case, however, the thickness is unknown, therefore we must rely on literature values for the material densities which is one source of error in the resulting measurements.

Table 1. Summary of densities for PCBM and P3HT. All values are in g/cm^3 .

PCBM	Reference	P3HT	Reference
1.64	[17,18]	1.16	[17]
1.61	[17]	1.15	[18,19]
1.60	[17]	1.12	[20]
1.58	[17]	1.1	[20,21]
1.5	[21–23]		
1.33	[19]		
1.25	[19]		

In order to measure this density difference, another EELS image was obtained in the same area and the carbon core loss edge was recorded. For each spectrum, the background was subtracted and the carbon areal density was calculated based on scattering probability as outlined in the data analysis section. An example spectrum, fit with a hydrogenic model, is shown in Figure 4. The analyzed spectrum image is shown in Figure 3b where the x and y coordinates are the position on the sample and the color represents carbon areal density.

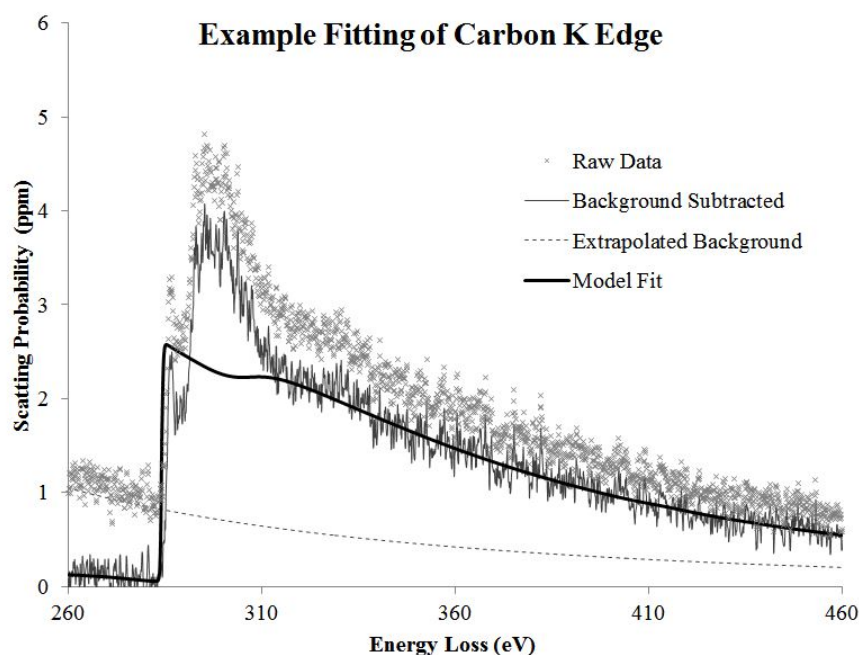


Figure 4. Example fit of a single spectrum within the BJH shown in Figure 1. The background model was fit within the energy range 256–281 eV and the hydrogenic model was fit excluding the range between 279 and 334 eV.

The similarity between Figure 3a and Figure 3b is clear. There is a higher carbon density in the same locations where the plasmon peak shifts to higher energy. The only area in which they disagree is in the surface layer. The carbon density map shows low carbon density indicating little PCBM while the plasmon peak position map shows a PCBM-like shift. This layer is indeed the protective platinum layer deposited during the focused ion beam (FIB) sample preparation and is a good illustration of the importance of verifying measurements through multiple independent techniques. Another advantage of using carbon density for distinguishing composition is that it is relatively insensitive to beam damage. Even if the polymers are damaged (bonds are broken and the sample chemically altered) during the data acquisition, the amount of carbon present in the sample will not change. However, one of the challenges of this technique is carbon contamination during data acquisition, *i.e.*, the build up of additional carbon on the surface of the sample will mask the carbon variations. Hence, extreme care must be taken to ensure a contamination free experimental environment.

4. Phase Ratio Mapping

With a carbon density map a further quantification becomes possible, namely the ratio of the component materials under the beam. In order to obtain this information we must know the thickness of the sample. If we know the thickness and we know the carbon density of the materials involved, we can calculate the fraction of each component present through a linear combination of the predicted carbon density.

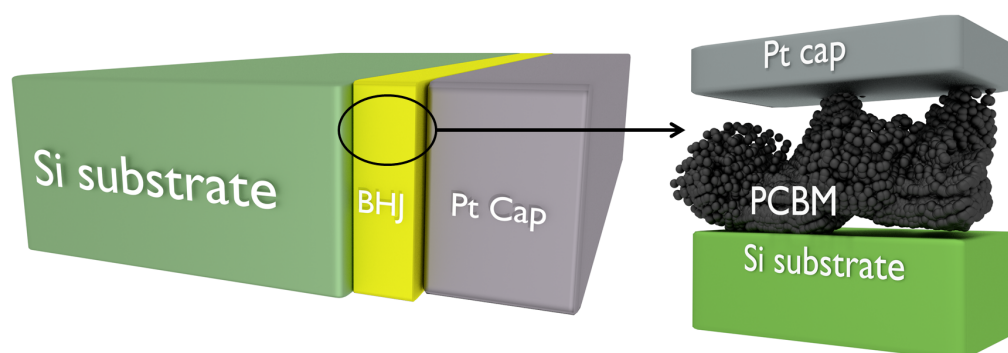


Figure 5. Conceptual diagram to aid understanding of the equations. The left-hand diagram is oriented perpendicular to the beam which traverses the sample vertically. We assume P3HT occupies some thickness within the BHJ (t_{P3HT}) and that the rest of the BHJ is occupied by PCBM (t_{PCBM}). In general, the total thickness of the sample is $t_{tot} = t_{P3HT} + t_{PCBM}$. In certain areas of the BHJ, however, the beam will go through either all P3HT (near the Pt cap) or all PCBM (near the Si substrate). In these cases, the total sample thickness becomes $t_{tot} = t_{P3HT}$ and $t_{tot} = t_{PCBM}$ respectively.

Let ρ_{P3HT} and t_{P3HT} be the carbon density and thickness of the P3HT, and ρ_{PCBM} and t_{PCBM} be the carbon density and thickness of the PCBM. $\rho_x t_x$ is then the carbon areal density we would measure for material x . In general, our measurement, M , is comprised of two parts:

$$\chi \rho_{P3HT} t + (1 - \chi) \rho_{PCBM} t = M \tag{2}$$

Here, χ represents the volume fraction of P3HT and is precisely what we would like to determine at every point on the sample. The only other unknown in this equation is t , the thickness of the sample.

In order to get a measurement of t , we must meet three criteria.

- The area of interest over which the spectrum image is acquired must be of uniform thickness.

In order to ensure this criterion is met as close as possible, the sample was prepared in a FIB with the specific intention of making the front and back faces coplanar, the width of the junction under examination is only about 100 nm, and Zero filtered imaging shows little thickness variation. With the addition of the sulfur signal this criterion can be removed as discussed later.

- There are some areas of pure material.

This criterion is rather restrictive. It requires that the feature sizes within the junction (*i.e.*, the phase separated domain sizes) are at least as large as the thickness of the sample. This requires large domain sizes which are not representative of the ideal OPV structure. Many samples investigated did not meet this criterion and could not be analyzed with this first method. With the addition of the sulfur signal this assumption can be removed as discussed later.

- The sample is contamination free.

Naturally, any contamination build-up during data acquisition will alter the carbon signal. We acquired images before and after the EELS acquisition to verify that contamination was not present.

If these three criterion are met, then in the areas of highest and lowest carbon concentration, Equation (2) simplifies since χ is either 0 or 1 (making use of the presence of pure material). The areas with the highest carbon density are pure PCBM while the areas with the lowest carbon density are pure P3HT. This is expressed as:

$$\rho_{P3HT}t_{P3HT} = M_{P3HT} \quad (3)$$

and,

$$\rho_{PCBM}t_{PCBM} = M_{PCBM} \quad (4)$$

where M_{P3HT} and M_{PCBM} are the measured areal densities of the highest and lowest value pixels within the junction (*i.e.*, taken from the data in Figure 3b in locations where the beam is actually within the junction not on the Pt cap). We can then use the literature densities and our measurements to obtain the sample thickness. If the three criterion are indeed met, we should find that $t_{P3HT} = t_{PCBM} = t$. Indeed we find from the pure PCBM regions a thickness value of 65 nm and from the pure P3HT regions a thickness value of 66 nm. Their close agreement indicates that the criterion were met acceptably well.

Taking the thickness of the sample to be 65 nm (changing the sample thickness from 65 to 66 nm does not lead to any significant change in the result) the carbon density map (Figure 3b) can be re-interpreted as a phase ratio map by solving Equation (2) for χ and inserting the measured carbon areal densities into M :

$$\chi = \frac{M - \rho_{PCBM}t}{\rho_{P3HT}t - \rho_{PCBM}t} \quad (5)$$

Figure 6 shows the carbon densities re-interpreted as a fraction of P3HT. What we immediately see from this picture is that we have a large amount of mixed material that is always present between the pure phases. There are three possibilities that may account for this. The first possibility is that the transition region from one material to the other is not perpendicular to the electron beam which will make a sharp transition appear much smoother. This option, although possible, seems unlikely since we do not see a sharp transition anywhere. If the mixed material was simply due to overlapping domains, we would expect to get a sharp transition somewhere. Alternatively, fractal-like structure with well defined (sharp) boundaries yet decreasing in feature size could also produce a similar component profile. The third possibility, which may not actually be much different from the second except in how it is expressed, is that there is a mixed phase composed of both P3HT and PCBM. There is mounting evidence that such a mixed phase exists [7,24–26]. Treat *et al.* (2011) [26] observed quick diffusion of PCBM into the amorphous areas of P3HT, suggesting that, though crystalline P3HT is immiscible with PCBM, amorphous P3HT readily mixes upon heating. Pfannmüller *et al.* (2011) [7]

observed such a mixed phase employing EFTEM imaging and a nonlinear multivariate statistical analysis. They found that the mixed phase decreases device performance due to a decrease in charge separation. Tvingstedt *et al.* (2010) [25], and Zhang *et al.* (2012) [24] also uncovered evidence for the presence and detriment of a mixed phase through the use of photoluminescent spectroscopy and near-infrared femtosecond transient absorption spectroscopy. Therefore it seems most likely that what we are observing in Figure 6 is a mixed phase between the pure domains of P3HT and PCBM.

In Figure 6, the average P3HT fraction is 0.536. This is quite close to the value expected based on our fabrication parameters of 0.555.

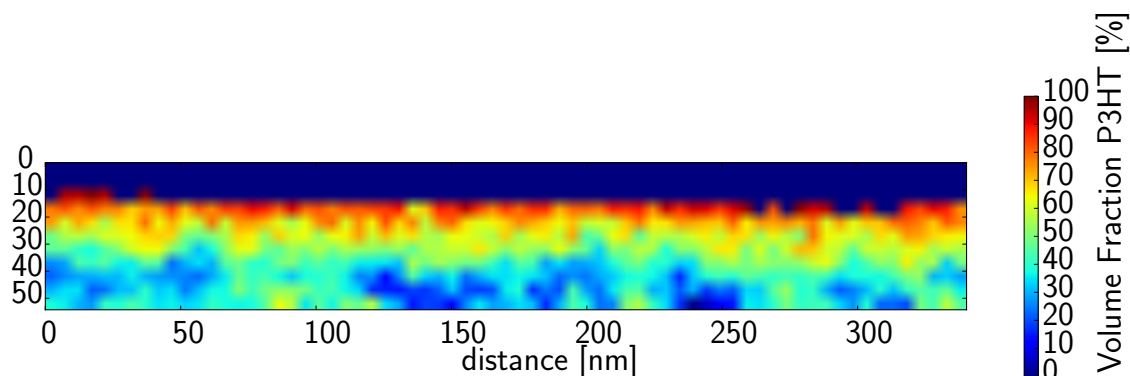


Figure 6. Data from Figure 3b re-interpreted as a fraction of P3HT. In some areas Equation (5) produces false values (above 100%) due to the low carbon concentration in the Pt cap toward the top. In these cases, it is not a physical result. These values have been set to zero.

5. PTB7/PCBM System: Results and Discussion

5.1. Density Measurement

We found no previously reported literature value for the density of PTB7. The density of PTB7 was obtained by measuring neutron scattering length density (nSLD) of spun-cast PTB7 film using neutron reflectivity. In nSLD, β is defined as,

$$\beta = N_a \rho_m \sum_{k=1}^n \frac{b_k}{m_{a,k}} \quad (6)$$

where N_a and ρ_m are Avogadro's number (mol^{-1}) and the mass density of the material (g/cm^3), b_k and $m_{a,k}$ are the coherent neutron scattering length (fm) [27] and atomic mass (g/mol) of the k^{th} atom in a molecule with total n atoms. The obtained mass density of PTB7 was found to be $1.17 \text{ g}/\text{cm}^3$.

5.2. Quantitative Elemental Mapping

An EELS image was obtained from a PTB7/PCBM phase separated cross section sample and the carbon K edge and sulfur L_{23} edge were recorded. For each spectrum, the background was subtracted and the carbon areal density was calculated based on scattering probability as outlined in the Data Analysis Section. The resulting images are shown in Figure 7.

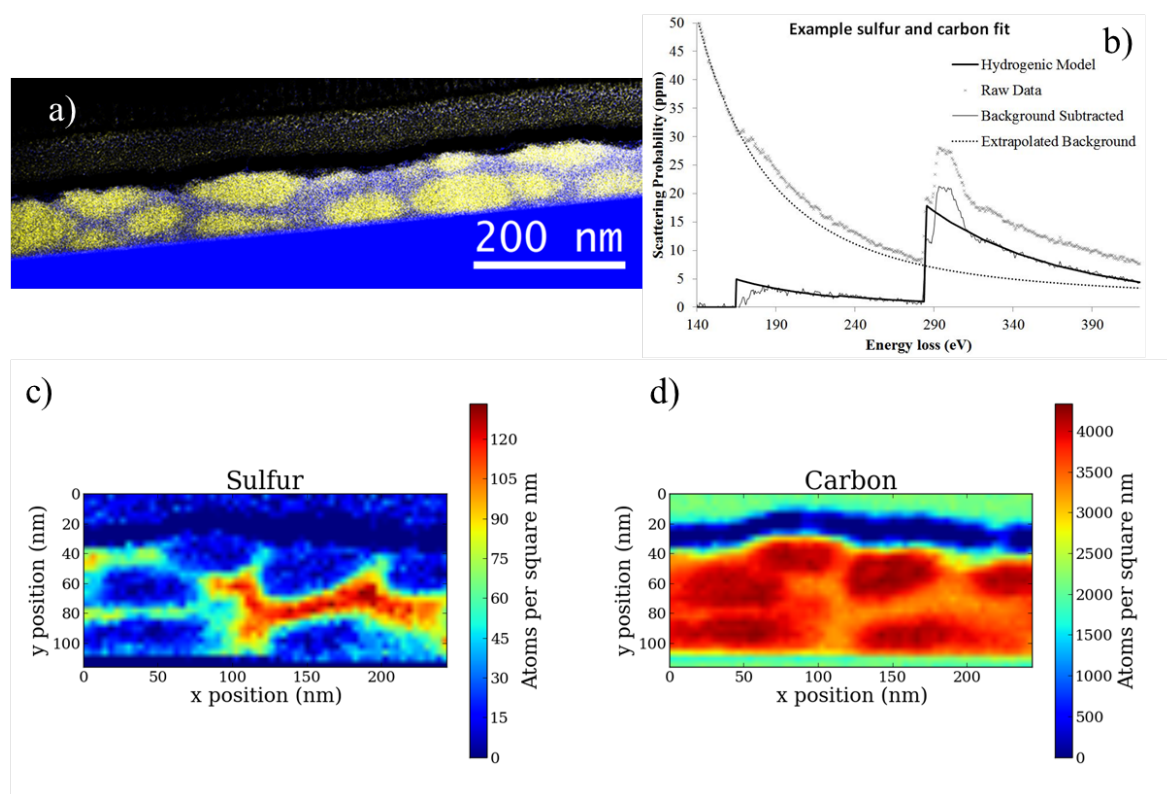


Figure 7. (a) EFTEM image for baseline comparison; (b) Example fit of sulfur L₂₃ and carbon K edge; (c) Carbon areal density in atoms/nm². The features shown in the EFTEM image are clearly visible in the carbon density variations. The layer with no carbon content is a gold layer; (d) Sulfur areal density in atoms/nm². Sulfur is only found in PTB7. This agrees nicely with the EFTEM image and the carbon areal density map. We clearly have qualitative agreement between the sulfur and carbon areal density maps which show similar features to the EFTEM image.

Figure 7c,d are clearly complementary and agree well with the morphology observed in the corresponding EFTEM image 7a. The sulfur signal denotes the PTB7 while the high carbon density denotes the PCBM.

5.3. Mathematical Description

Further refinement of this technique is possible with the additional information provided by the sulfur signal present in many of the donor polymers used in OVPs such as PTB7, which has a sulfur density of 3.72 atoms/nm³. Specifically, two additional ways to calculate the volume fraction of the component materials become available. The first is to use the thickness obtained from Equation (3) or (4) and calculate what the sulfur signal should be in a pure PTB7 area. For example, if the sample was 100 nm thick, given a sulfur density of 3.72 atoms/nm³, we would expect an atomic areal density of 372 atoms/nm². We can then divide our actual measurement by this value to obtain a fraction of the predicted total. We express this as

$$\chi = \frac{M_S}{M_{S_{tot}}} \quad (7)$$

where M_S is our measured sulfur areal density, and $M_{S_{tot}}$ is the total predicted sulfur areal density for a pure PTB7 region given a known sample thickness. This is not much better than the previous method for calculating volume fraction since it still works under the criteria that the sample must be of uniform thickness and there must be a pure area to measure the sample thickness. This is not surprising since here we are simply using the sulfur signal instead of the carbon signal.

The third way to calculate volume fraction is by making use of both the carbon and sulfur signal together. In general, the carbon signal is composed of two parts, the PCBM part and the PTB7 part. The sulfur signal, however, comes only from the PTB7. We can, therefore, use the sulfur signal to predict how much of the carbon signal is from PTB7. The sulfur signal can be written

$$M_S = \rho_S t_{PTB7} \quad (8)$$

where M_S is the measured sulfur areal density, ρ_S is the density of sulfur in PTB7, and t_{PTB7} is the thickness of the PTB7 (not the total thickness). We can then solve for t_{PTB7} and use it in the carbon relation

$$M_{PTB7} = \rho_{PTB7} t_{PTB7} \quad (9)$$

where M_{PTB7} is the unknown component of the carbon signal due to PTB7 and ρ_{PTB7} is the carbon density of PTB7. The ratio of M_{PTB7} to the total carbon signal measured gives the fraction of PTB7 in the film.

$$\chi = \frac{M_{PTB7}}{M} = \frac{\rho_{PTB7} t_{PTB7}}{M} = \frac{\rho_{PTB7} M_S}{\rho_S M} \quad (10)$$

Here, we note that the dependence on sample thickness has been eliminated through the use of two independent measurements. This also eliminates the requirement for there to exist some area of pure material on which to take a thickness measurement. In fact, once the ratio of the component materials is determined, we may calculate a thickness for every pixel in our spectrum image based on the carbon areal density with the following equation.

$$t = \frac{M\chi}{\rho_{PTB7}} + \frac{M(1-\chi)}{\rho_{PCBM}} \quad (11)$$

This measurement becomes handy because Equations (5) and (7) both need a thickness input that was originally acquired by assuming pure material somewhere on the sample and also assuming uniform thickness. By using Equation (11) for the thickness, we eliminate both requirements for Equations (5) and (7). In fact, Equations (5) and (7) actually become identical when Equation (11) is used for the thickness.

5.4. Comparing the Models

We used the variable thickness from Equation (11) to generate a thickness map (Figure 8a) and then used this map as input into Equations (5) and (7) (which result in the same expression) to form the PTB7 volume fraction map shown in Figure 8b. Figure 8c shows the PTB7 volume fraction map obtained from the combined sulfur and carbon signal from Equation (10). We note that they both show the same overall structure and agree with each other to about 10%–20%. One feature that is common is that there is no pure PTB7 anywhere. This is not evident from examining the EFTEM image shown in Figure 7a. In the EFTEM image, it appears as though we have PCBM aggregates in a PTB7 matrix. One might be led to infer that the PTB7 areas are pure. Instead, we see that the maximum PTB7 concentration is between 49% and 64%. This implies that what we are actually seeing is an interconnected network of PTB7 in a matrix of PCBM. Another clue that this is the correctly interpreted device morphology is that the PCBM aggregates implied by EFTEM imaging are entirely separated from one another. This would prevent any appreciable functioning of the device and yet we observed a PCE of 5.2%.

The PTB7 average fraction in Figure 7b,c was found to be 0.304 and 0.190, respectively. The expected fraction based on our fabrication parameters is 0.4 indicating that either we have investigated a non-representative area of the sample, or use of an FIB for sample preparation may be

attributing to a loss of S from the PTB7. Further investigations into the accuracy and reproducibility of this characterization method are warranted to fully explore the strengths and weaknesses.

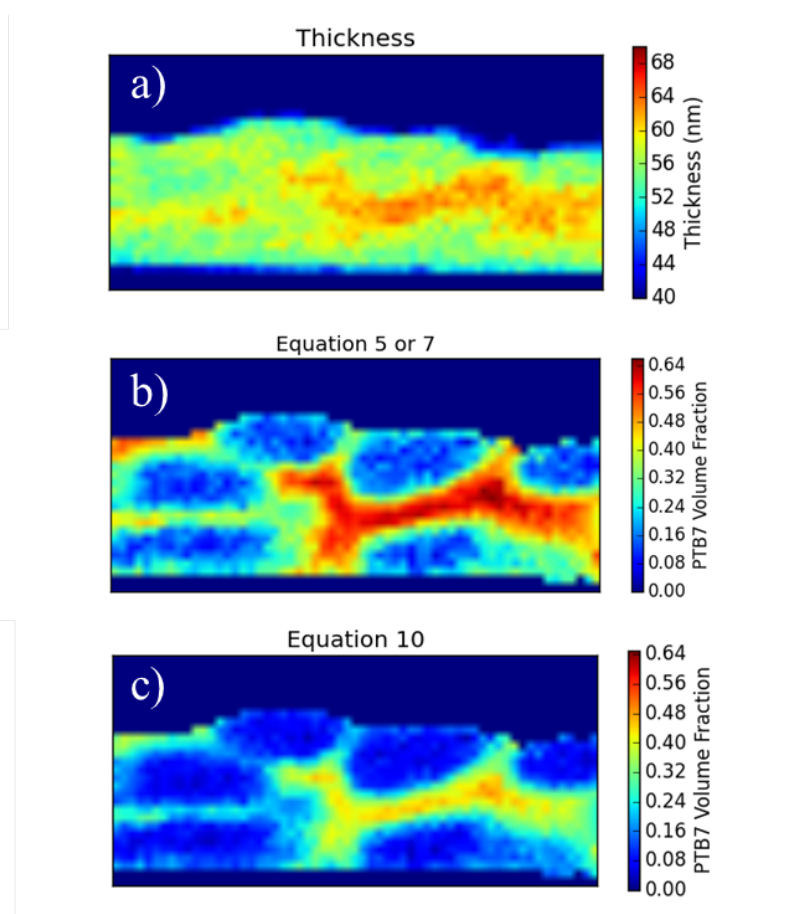


Figure 8. (a) Thickness map based on Equation (11). Most values lie between 55 and 65 nm; (b) Volume fraction of PTB7 based on Equations (5) or (7) using the variable thickness (from (a)), in lieu of assuming a constant thickness; (c) Volume fraction of PTB7 based on both the sulfur and carbon signal Equation (10). We see agreement within about 10%–20%.

5.5. Sources of Error

Agreement between the equations of only 10%–20% is not surprising since we know that we have a few uncertainties in our measurements. One source of error is uncertain material densities, mentioned earlier. Variation in reported densities may not just be errors in measurement but rather actual variation in density of the material based on processing parameters. For example, the P3HT density in the mixed phase is not necessarily the same as amorphous (or crystalline) P3HT. None of these variabilities are taken into account. Table 1 shows the range of values found in the literature for P3HT and PCBM densities. The density for PTB7 was not found in the literature, which prompted our own measurements.

A second source of error is in the fitting of the sulfur signal. The sulfur concentration is fairly low and this results in a small signal on top of a relatively large background (see Figure 7b). The smaller the signal, the more uncertain is the measurement. This could lead to inaccurate representations particularly in the PCBM regions (PCBM has no sulfur) and, indeed, in the thickness map (Figure 8a) we see slight structure that follows the PTB7 structure which may be introduced by the sulfur fitting. It is unlikely that this thickness variation truly exists.

A third, less pronounced, source of error is in fitting the carbon signal. This is a strong signal, well above the background, so it is likely that errors arising from improper fitting of the carbon signal are relatively small.

A fourth possible source of error is that FIB milling may create a thin, dense, amorphous carbon layer on the surfaces. This is not taken into account in any of the equations and should have some effect on the calculated volume fractions. How much is, at this point, unknown.

6. Conclusions

We have shown two methods for component material detection in OPV systems, namely EELS imaging for plasmon peak position mapping and EELS imaging for core loss elemental concentration mapping. The plasmon peak position mapping relies on plasmon position shifts that are well established for EFTEM imaging but, to the author's knowledge, no quantitative position mapping across a sample has been done. Such a map gives slightly more detailed information about the sample because each spectrum can be analyzed independently post-acquisition for possible artifacts.

EELS image analysis for quantitative carbon and sulfur concentration mapping demonstrated component detection capabilities due to the elemental density differences between P3HT and PTB7, and PCBM.

We further demonstrated that the carbon areal density map may be transformed into a component ratio map which offers a much more useful quantification of the data. This requires that the sample thickness be known, which we demonstrated can be obtained from the carbon areal density map with a few assumptions, or from the combined carbon and sulfur areal densities. The component ratio map may be employed to determine the sharpness of the component separation as well as the purity of the separated phases which will have significant impact on device performance.

The ability to interpret core loss EELS images in terms of absolute atomic density has much farther-reaching applications than just OPV characterization. It could be used in studies on block copolymers, ionomers, or other biological samples. It could be used to determine impurity concentrations, atomic ratios, or ratios of composite materials. Moreover, once the data is converted to atomic density, rather than counts, different experiments under different conditions in different microscopes may be compared to each other.

Acknowledgments: This research has been made possible through funding by the Sustainable Energy and Education Research Center (SEERC), Tennessee Solar Conversion and Storage using Outreach, Research and Education (TN-SCORE), the Department of Energy, Basic Energy Sciences (DOE-BES) Some part of this research was conducted at the Center for Nanophase Materials Sciences (CNMS), a DOE Office of Science User Facility.

Author Contributions: Ondrej Dyck: Principle author and TEM specialist and performed all TEM related data collection and analysis as well as TEM sample preparation. Sheng Hu: Prepared P3HT:PCBM films for TEM experiments and performed all non-TEM related measurements and experiments related to the P3HT:PCBM system. Sanjib Das: Prepared PTB7:PCBM films for TEM experiments, and fabricated devices. Jong Keum: Contributed to discussion and data analysis with Sanjib Das. Kai Xiao: Direct supervisor for Sanjib Das. Bamin Khomami: PhD adviser for Sheng Hu. Gerd Duscher: PhD adviser for Ondrej Dyck.

Conflicts of Interest: The authors declare no conflict of interest.

References

1. Dang, M.T.; Hirsch, L.; Wantz, G. P3HT:PCBM, Best seller in polymer photovoltaic Research. *Adv. Mater.* **2011**, *23*, 3597–3602.
2. Chen, W.; Nikiforov, M.P.; Darling, S.B. Morphology characterization in organic and hybrid solar cells. *Energy Environ. Sci.* **2012**, *5*, 8045–8074.
3. Darling, S.B.; You, F. The case for organic photovoltaics. *RSC Adv.* **2013**, *3*, 17633–17648.
4. Nicholson, P.G.; Castro, F.A. Organic photovoltaics: Principles and techniques for nanometre scale characterization. *Nanotechnology* **2010**, *21*, 492001.
5. Herzing, A.A.; Richter, L.J.; Anderson, I.M. 3D nanoscale characterization of thin-film organic photovoltaic device structures via spectroscopic contrast in the TEM. *J. Phys. Chem. C* **2010**, *114*, 17501–17508.

6. Drummy, L.F.; Davis, R.J.; Moore, D.L.; Durstock, M.; Vaia, R.A.; Hsu, J.W.P. Molecular-scale and nanoscale morphology of P3HT:PCBM bulk heterojunctions: Energy-filtered TEM and low-dose HREM. *Chem. Mater.* **2011**, *23*, 907–912.
7. Pfannmöller, M.; Flügge, H.; Benner, G.; Wacker, I.; Sommer, C.; Hanselmann, M.; Schmale, S.; Schmidt, H.; Hamprecht, F.A.; Rabe, T.; *et al.* Visualizing a homogeneous blend in bulk heterojunction polymer solar cells by analytical electron microscopy. *Nano Lett.* **2011**, *11*, 3099–3107.
8. Schindler, W.; Wollgarten, M.; Fostiropoulos, K. Revealing nanoscale phase separation in small-molecule photovoltaic blends by plasmonic contrast in the TEM. *Org. Electron.* **2012**, *13*, 1100–1104.
9. Kozub, D.R.; Vakhshouri, K.; Orme, L.M.; Wang, C.; Hexemer, A.; Gomez, E.D. Polymer crystallization of partially miscible polythiophene/fullerene mixtures controls morphology. *Macromolecules* **2011**, *44*, 5722–5726.
10. Huang, Y.; Kramer, E.J.; Heeger, A.J.; Bazan, G.C. Bulk heterojunction solar cells: Morphology and performance relationships. *Chem. Rev.* **2014**, *114*, 7006–7043.
11. Brady, M.A.; Su, G.M.; Chabynyc, M.L. Recent progress in the morphology of bulk heterojunction photovoltaics. *Soft Matter* **2011**, *7*, 11065–11077.
12. Hu, S.; Dyck, O.; Chen, H.; Hsiao, Y.c.; Hu, B.; Duscher, G.; Dadmun, M.; Khomami, B. The impact of selective solvents on the evolution of structure and function in solvent annealed organic photovoltaics. *RSC Adv.* **2014**, *4*, 27931–27938.
13. Das, S.; Keum, J.K.; Browning, J.F.; Gu, G.; Yang, B.; Dyck, O.; Do, C.; Chen, W.; Chen, J.; Ivanov, I.N.; *et al.* Correlating high power conversion efficiency of PTB7:PC₇₁BM inverted organic solar cells with nanoscale structures. *Nanoscale* **2015**, *7*, 15576–15583.
14. Egerton, R.F. *Electron Energy-Loss Spectroscopy in the Electron Microscope*; Springer: New York, NY, USA, 2011.
15. Tougaard, S. Universality classes of inelastic electron scattering cross-sections. *Surface Interface Anal.* **1997**, *25*, 137–154.
16. Nikiforov, M.P.; Lai, B.; Chen, W.; Chen, S.; Schaller, R.D.; Strzalka, J.; Maser, J.; Darling, S.B. Detection and role of trace impurities in high-performance organic solar cells. *Energy Environ. Sci.* **2013**, *6*, 1513–1520.
17. Ro, H.W.; Akgun, B.; O'Connor, B.T.; Hammond, M.; Kline, R.J.; Snyder, C.R.; Satija, S.K.; Ayzner, A.L.; Toney, M.F.; Soles, C.L.; *et al.* Poly(3-hexylthiophene) and [6,6]-phenyl-C61-butyric acid methyl ester mixing in organic solar cells. *Macromolecules* **2012**, *45*, 6587–6599.
18. Tada, A.; Geng, Y.; Wei, Q.; Hashimoto, K.; Tajima, K. Tailoring organic heterojunction interfaces in bilayer polymer photovoltaic devices. *Nat. Mater.* **2011**, *10*, 450–455.
19. Kiel, J.W.; Kirby, B.J.; Majkrzak, C.F.; Maranville, B.B.; Mackay, M.E. Nanoparticle concentration profile in polymer-based solar cells. *Soft Matter* **2010**, *6*, 641–646.
20. Prosa, T.J.; Winokur, M.J.; Moulton, J.; Smith, P.; Heeger, A.J. X-ray structural studies of poly(3-alkylthiophenes): An example of an inverse comb. *Macromolecules* **1992**, *25*, 4364–4372.
21. Sun, Y.; Han, Y.; Liu, J. Controlling PCBM aggregation in P3HT/PCBM film by a selective solvent vapor annealing. *Chin. Sci. Bull.* **2013**, *58*, 2767–2774.
22. Bulle-Lieuwma, C.; van Gennip, W.; van Duren, J.; Jonkheijm, P.; Janssen, R.; Niemantsverdriet, J. Characterization of polymer solar cells by TOF-SIMS depth profiling. *Appl. Surface Sci.* **2003**, *203–204*, 547–550.
23. Geens, W.; Martens, T.; Poortmans, J.; Aernouts, T.; Manca, J.; Lutsen, L.; Heremans, P.; Borghs, S.; Mertens, R.; Vanderzande, D. Modelling the short-circuit current of polymer bulk heterojunction solar cells. *Thin Solid Films* **2004**, *451–452*, 498–502.
24. Zhang, W.; Hu, R.; Li, D.; Huo, M.M.; Ai, X.C.; Zhang, J.P. Primary dynamics of exciton and charge photogeneration in solvent vapor annealed P3HT/PCBM films. *J. Phys. Chem. C* **2012**, *116*, 4298–4310.
25. Tvingstedt, K.; Vandewal, K.; Zhang, F.; Inganäs, O. On the dissociation efficiency of charge transfer excitons and frenkel excitons in organic solar cells: A luminescence quenching study. *J. Phys. Chem. C* **2010**, *114*, 21824–21832.
26. Treat, N.D.; Brady, M.A.; Smith, G.; Toney, M.F.; Kramer, E.J.; Hawker, C.J.; Chabynyc, M.L. Interdiffusion of PCBM and P3HT reveals miscibility in a photovoltaically active blend. *Adv. Energy Mater.* **2011**, *1*, 82–89.
27. Sears, V.F. Neutron scattering lengths and cross sections. *Neutron News* **1992**, *3*, 26–37.

